Scientific Research Publishing

Advances in Materials Physics and Chemistry, 2026, 16(9), 333-353
https://www.scirp.org/journal/ampc
ISSN Online: 2162-5328
ISSN Print: 2162-531X

Comparative Study of Crystallite Size and Microstrain of Synthesized Analcime Using X-Ray Diffraction Profile Analysis

Ferland Ngoro-Elenga[1,2*], Fernand Atipo Itoua Ngopoh[1], Eric Ziki[3], Merveilla Bounzi[1], Hilaire Elenga[2], Timothée Nsongo[2]

[1]Laboratory of Inorganic and Applied Chemistry, Marien Ngouabi University, Brazzaville, Congo
[2]Geological and Mining Research Center, Ministry of Mining Industries and Geology, Brazzaville, Congo
[3]Laboratory of Crystallography and Molecular Physics, Félix Houphouët-Boigny University, Abidjan, Côte d'Ivoire
Email: *ferland.ngoro-elenga@umng.cg

How to cite this paper: Ngoro-Elenga, F., Atipo Itoua Ngopoh, F., Ziki, E., Bounzi, M., Elenga, H. and Nsongo, T. (2026) Comparative Study of Crystallite Size and Microstrain of Synthesized Analcime Using X-Ray Diffraction Profile Analysis. *Advances in Materials Physics and Chemistry*, **16**, 333-353.
https://doi.org/10.4236/ampc.2026.169019

Received: July 23, 2026
Accepted: September 8, 2026
Published: September 11, 2026

Abstract

The present study consisted of a comparative investigation of crystallite size and microstrain through the analysis of X-ray diffraction peak broadening of analcime synthesized by the hydrothermal method. Several characterization techniques, including X-ray diffraction (XRD), scanning electron microscopy coupled with energy-dispersive spectroscopy (SEM/EDS), Fourier transform infrared spectroscopy (FTIR), and X-ray fluorescence (XRF), were employed to characterize the synthesized material. XRD analysis revealed the presence of a single phase corresponding to analcime. SEM analysis revealed a trapezohedral or deltoidal icositetrahedral morphology, while EDS confirmed the presence of the expected elements accross the analyzed regions, with some local variations in their relative abundances. XRF analysis demonstrated the aluminosilicate nature of the material with a Si/Al ratio of 2.8, while FTIR spectroscopy revealed absorption bands in the range 500 - 1000 cm^{-1}, characteristic of zeolitic materials. Several XRD peak broadening analysis methods were applied, including the Scherrer, Monshi-Scherrer, Williamson-Hall, size-strain plot, Halder-Wagner, and modified Warren-Averbach methods. The results highlight significant differences in crystallite size and microstrain values, arising from the assumptions specific to each model. The Scherrer and Monshi-Scherrer methods provided crystallite size estimates ranging from 75.47 nm to 98.71 nm. The UDM, USDM, and UDEDM approaches of the Williamson-Hall method revealed crystallite sizes of 158.54 nm, 149.46 nm, and 155.21 nm, respectively, with corresponding microstrain values of 0.931×10^{-3}, 0.902×10^{-3}, and 0.924×10^{-3}. The Halder-Wagner, size-strain plot, and modified Warren-Averbach methods yielded crystallite sizes of 115.54 nm, 115.54 nm,

and 128.38 nm, respectively, and microstrain values of 1.02×10^{-3}, 6.26×10^{-3}, and 8.13×10^{-4}.

Keywords

Analcime, X-Ray Diffraction, Crystallite Size, Microstrain, Microstructure

1. Introduction

Zeolites are microporous crystalline aluminosilicate materials characterized by an open framework structure containing cavities and channels occupied by exchangeable ions (Na^+, K^+, Ca^{2+}) and water molecules. Among these materials, analcime is widely used because of its ion-exchange capacity, catalytic, and adsorption properties [1]-[3]. Hydrothermal synthesis is the most commonly employed method for the preparation of synthetic analcime, as it reproduces the natural formation conditions while allowing precise control of parameters such as temperature, treatment time, and the chemical composition of the initial hydrogel. It is described as a dissolution-recrystallization process involving aluminosilicate precursors. The formation of analcime is strongly influenced by the Si/Al molar ratio, the base concentration, and the dissolution-recrystallization rate of these precursors [4]. The existence of hybrid mechanisms combining classical and non-classical pathways involving amorphous aggregates or aluminosilicate gels has been highlighted by several studies [5]-[8]. These observations challenge the simplified view of homogeneous crystal growth and emphasize the critical role of nucleation stages. The literature review reveals significant variability in crystallite sizes and morphologies under similar synthesis conditions. Crystallite size and lattice microstrain are strongly influenced by the synthesis conditions. One study reported that the average crystallite size of analcime can reach approximately 150 nm depending on the hydrothermal conditions and the structure-directing agents employed [9]. In this context, the estimation of crystallite size can no longer be regarded as a simple descriptive measurement, but rather as an indirect tool for understanding the material formation mechanisms. Therefore, the characterization of these microstructural parameters mainly relies on the analysis of X-ray diffraction profiles, where peak broadening may arise from the combined contributions of crystallite size and lattice microstrain. However, several mathematical approaches and methods, such as the Scherrer, Williamson-Hall, Size-Strain Plot, Halder-Wagner, and Warren-Averbach methods, have been employed in numerous studies [10]-[13]. In this context, the Scherrer method is the simplest and most widely used approach for estimating the average crystallite size from diffraction peak broadening without considering the contribution of strain. The Williamson-Hall method is one of the most commonly applied approaches for estimating crystallite size, stress, lattice strain, and strain energy density. This method is subdivided into three models: the uniform deformation model (UDM), the uniform

stress deformation model (USDM), and the uniform deformation energy density model (UDEDM) [14] [15]. The size-strain plot and Halder-Wagner methods introduce a more realistic modeling of diffraction profiles by assuming specific distributions (Gaussian and Lorentzian) of size and strain effects, thereby improving the reliability of the extracted parameters. Finally, the Warren-Averbach method, based on the Fourier analysis of diffraction profiles, constitutes a more rigorous approach that allows the separate determination of coherent domain size and microstrain distribution [16]-[18]. However, this method requires high-quality experimental data and more complex mathematical processing, thereby limiting its systematic use. Despite the diversity of these methods, few comparative studies have been devoted to the critical evaluation of these different approaches applied to hydrothermally synthesized analcime. In this context, the objective of the present study is to investigate the microstructural properties (crystallite size and lattice microstrain) of synthetic analcime through the analysis of X-ray diffraction peak broadening using the Scherrer, Monshi-Scherrer, Williamson-Hall (UDM, USDM, UDEDM), size-strain plot, Halder-Wagner, and modified Warren-Averbach approaches.

2. Expérimentation

2.1. Hydrothermal Synthesis of the Zeolitic Material

The zeolitic compound was synthesized by mixing 1.64 g of sodium aluminate with 50 mL of an aqueous sodium hydroxide solution at a concentration of 0.103 g/mL. After 10 minutes of stirring, 11.1 mL of sodium silicate was added to the previous solution under vigorous magnetic stirring to form the gel. After 24 hours of aging, the formed aluminosilicate gel was transferred into an autoclave, which was then placed in an oven at 105˚C for 8 days. After crystallization, the obtained product was recovered, washed with distilled water until pH = 9, and dried at 95˚C for 24 hours.

2.2. Characterization Methods of the Synthesized Powder

The synthesized product was analyzed using several techniques. X-ray diffraction (XRD) measurements were carried out using an X'Pert3 Panalytical powder diffractometer employing Cu Kα radiation with wavelengths of ($\lambda K\alpha 1$ = 1.54059 Å; $\lambda K\alpha 2$ = 1.54441 Å). The data were collected under the following experimental conditions: $5 \le 2\theta \le 50^\circ$, $\Delta 2\theta = 0.02^\circ$, 45 kV and 100 mA. Phase identification was performed using the QualX software with the COD database. Rietveld profile refinement was carried out using the FullProf program (version: March 2021). The profile function used was the Thompson-Cox-Hastings pseudo-Voigt convoluted with axial divergence asymmetry. The average crystallite size and microstrain were estimated using the Scherrer, Monshi-Scherrer, Williamson-Hall, Halder-Wagner, Size-Strain Plot, and modified Warren-Averbach methods. The instrumental broadening of the XRD peaks was determined using a crystalline silica standard, for which an instrumental FWHM, $\beta_{\text{instrumental}}$, of 0.071˚ was measured

for the (1 1 1) reflection at $2\theta = 28.4^{\circ}$. The instrumental contribution was corrected using a Gaussian deconvolution procedure according to $\beta^2_{\text{correted}} = \beta^2_{\text{obs}} - \beta^2_{\text{instrumental}}$, where β_{obs} is the observed FWHM. The profiles of the individual XRD reflections were fitted in OriginPro 2024 software using a Gaussian function to determine the peak positions and FWHM values. Only well-resolved reflections without significant overlap with neighboring peak were considered for the microstructural analysis and subsequent fitting procedures. The morphology and local elemental chemical composition were investigated using a Regulus 8100 scanning electron microscope coupled with energy-dispersive spectroscopy. Fourier-transform infrared analysis was performed on a Thermo Scientific Nicolet iS50 FTIR spectrophotometer scanning the range from 500 to 4000 cm^{-1}. The elemental composition was determined using a Thermo Fisher Scientific X-ray fluorescence spectrometer.

2.3. XRD Data Analysis

2.3.1. Scherrer and Monshi-Scherrer Methods

The Scherrer method is the simplest and most rapid approach for estimation the average crystallite size, as it neglects the contribution of lattice microstrian to X-ray diffraction peak broadening. This size is calculated using Equation (1) [14] [19] [20].

$$D = \frac{K \cdot \lambda}{\beta \cos\theta} \tag{1}$$

The Monshi-Scherrer method is a modified form of the Scherrer equation. In this approach, Equation (1) is linearized to yield the following expression Equation (2) [20]:

$$\ln\beta = \ln\left(\frac{K \cdot \lambda}{D}\right) + \ln\left(\frac{1}{\cos\theta}\right) \tag{2}$$

With D: average crystallite size (nm); K: Scherrer constant ($K = 0.9$); λ: X-ray wavelenght (nm); β: full width at half maximum (FWHM) corrected for instrumental broadening, in radians; θ: Bragg's angle in radians.

2.3.2. Williamson-Hall Methods

Williamson-Hall method considers X-ray diffraction peak broadening as a combinaison of crystallite size and lattice microstrain contributions. These microstrain are attributed to the presence of point defects, grains boundaries, and stacking faults [21] [22]. This broadening is defined as follows:

$$\beta_{hkl} = \beta_{\text{size}} + \beta_{\text{strain}} \tag{3}$$

Three models are derived from the Williamson-Hall method [20] [22] [23], namely:

a) Uniform Deformation Model

This model assumes that lattice microstrain is uniformly distributed in all crystallographic directions throughout the crystal, resulting in isotropic peak broadening. It is expressed by Equation (4) [13]:

$$\beta_{hkl}\cos\theta = \frac{K\cdot\lambda}{D} + 4\varepsilon\sin\theta \tag{4}$$

where ε is the lattice microstrain.

b) Uniform Stress Deformation Model

Unlike UDM, USDM takes into account the anisotropy of Young's modulus, thereby providing a more realistic description of the lattice deformation conditions. The stress associated with lattice microstrain is assumed to be uniform across all crystallographic directions, while explicitly incorporating the contribution of microstrain within the crystals. The following Equation (5) represents Hooke's law, which describes a linear relationship between strain and stress:

$$\varepsilon = \frac{\sigma}{Y_{hkl}} \tag{5}$$

where σ is the stress, ε is the anisotropic microstrain and Y_{hkl} is the modulus of elasticity or Young's modulus. By substituting ε with its expression from relation 5, the Williamson-Hall model can be rewritten as Equation (6) [24]:

$$\beta_{hkl}\cos\theta = \frac{K\cdot\lambda}{D} + 4\frac{\sigma}{Y_{hkl}}\sin\theta \tag{6}$$

For cubic systems, Young's modulus is given by Equation (7)

$$\frac{1}{Y_{hkl}} = S_{11} - 2\left(S_{11} - S_{12} - \frac{1}{2}S_{44}\right)\times\frac{\left(h^2k^2 + k^2l^2 + h^2l^2\right)}{\left(h^2 + k^2 + l^2\right)^2} \tag{7}$$

With:

$$S_{11} = \frac{C_{11} + C_{12}}{\left(C_{11} - C_{12}\right)\left(C_{11} + 2C_{12}\right)}; S_{12} = \frac{-C_{12}}{\left(C_{11} - C_{12}\right)\left(C_{11} + 2C_{12}\right)}; S_{44} = \frac{1}{C_{44}}$$

where:

C_{11}, C_{12}, C_{44} and S_{11}, S_{12}, S_{44} are the stiffness constants and the elastic compliances of cubic analcime zeolites, respectively. The values of the elastic constants C_{ij} have been reported in references [25] [26]; those used in this study are as follows: C_{11} = 112.5 GPa, C_{12} = 33.4 GPa, C_{44} = 27.9 GPa [25].

c) Uniform Deformation Energy Density Model

Unlike the UDM and USDM approaches, which assume isotropy and a linear relationship between strain and stress, respectively, the UDEDM approach considers the anisotropic deformation of the crystalline lattice in all crystallographic directions. This deformation is caused by the strain energy density [14] [22] [27]. This model, therefore, relies on the anisotropy of Young's modulus Y_{hkl}. Equation (8) gives Hooke's law relating the anisotropic strain energy density (u) to the stress. After rearrangement, the Williamson-Hall model can be expressed as Equation (9)

$$u = \varepsilon^2\cdot\frac{Y_{hkl}}{2} \tag{8}$$

$$\beta_{hkl}\cos\theta = \frac{K\cdot\lambda}{D} + 4\sin\theta\cdot\sqrt{\frac{2u}{Y_{hkl}}} \tag{9}$$

2.3.3. Size-Strain Plot Method

The Size-Strain Plot method allows the estimation of crystallite size and lattice strain by assuming that the broadening of the diffraction profile results from a combination of Lorentzian and Gaussian functions Equation (10), associated with crystallite size and microstrain, respectively.

$$\beta_{hkl} = \beta_L + \beta_G \tag{10}$$

where β_L and β_G are the full widths at half maximum of the Lorentzian and Gaussian functions, respectively. The relationship used to estimate the crystallite size and lattice strain by the Size-Strain Plot method is expressed by Equation (11) [10] [14] [28].

$$\left(d_{hkl} \cdot \beta_{hkl} \cdot \cos\theta\right)^2 = \frac{K \cdot \lambda}{D}\left(d_{hkl}^2 \cdot \beta_{hkl} \cdot \cos\theta\right) + \frac{\varepsilon^2}{4} \tag{11}$$

2.3.4. Halder-Wagner Method

In contrast to the size-strain plot method, which assumes that broadening due to crystallite size follows a Lorentzian function and that due to strain is described by a Gaussian function, the Halder-Wagner method assumes that XRD peak broadening is a symmetric Voigt function [29], *i.e.*, a convolution of a Lorentzian function and a Gaussian function [30]. In this case, Equation (12) gives the full width at half maximum:

$$\beta_{hkl}^2 = \beta_L \beta_{hkl} + \beta_G^2 \tag{12}$$

The relation used to determine the crystallite size and lattice strain, according to the Halder-Wagner method, is given by Equation (13) [22] [31]:

$$\left(\frac{\beta_{hkl}}{2\tan\theta}\right)^2 = \frac{K \cdot \lambda}{D}\left(\frac{\beta_{hkl}}{4\tan\theta \cdot \sin\theta}\right) + 4\varepsilon^2 \tag{13}$$

2.3.5. Modified Warren-Averbach Method

The Warren-Averbach method, based on the Fourier analysis of XRD peak profiles, enables the separation and quantification of crystallite size and lattice microstrain [20] [32]-[34]. A modified equation derived from this approach Equation (14) [20] [35] [36] was proposed without employing Fourier series analysis.

$$\frac{\beta_{hkl}^2}{\tan^2\theta} = \frac{\lambda}{D}\left(\frac{\beta_{hkl}}{\tan\theta\sin\theta}\right) + 25\left\langle\varepsilon^2\right\rangle \tag{14}$$

3. Results and Discussion

3.1. Structural Parameter

The XRD pattern of the synthesized product (**Figure 1**) reveals the presence of a pure phase consisting solely of analcime (COD card 00-900-8207), with space group I a -3 d and lattice parameter a = 13.74079 Å, characterized by peaks at 2θ (˚) = 15.76, 18.22, 24.20, 25.90, 30.48, 31.86, 33.20, 35.74, 36.96, 40.42, 41.52, 42.60, 44.68, 47.68, and 48.64. All peaks were indexed and correspond respectively to the reticular planes (2 1 1), (2 2 0), (3 2 1), (4 0 0), (3 3 2), (4 2 2), (4 3 1), (5 2 1), (4 4

0), (5 3 2), (6 2 0), (5 4 1), (6 3 1), (6 4 0), and (6 3 3). The most intense peak corresponds to the (4 0 0) plane; this feature has also been reported by [37] [38].

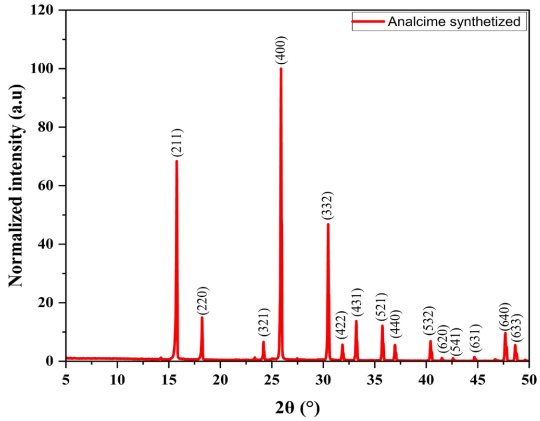

Figure 1. XRD pattern of synthetized zeolite.

3.2. Rietveld Refinement

Figure 2 shows the observed and calculated profiles along with their difference profile. The Rietveld refinement yielded agreement factors of Rp = 12.1% and Rwp = 12.6%, indicating a satisfactory overall fit between the experimental and calculated profiles [39] [40]. The low value of R_{Bragg} = 3.1% reflects the good quality of the structural model. However, the relatively high GoF value of 10.9 suggests a discrepancy between the experimental data and the refined model; this deviation may indicate the presence of contributions not accounted for in the refinement, such as preferred orientation effects, microstrain, or the presence of minor secondary phases [41] [42]. The low value of Rexp = 3.8 indicates the high quality of the experimental data.

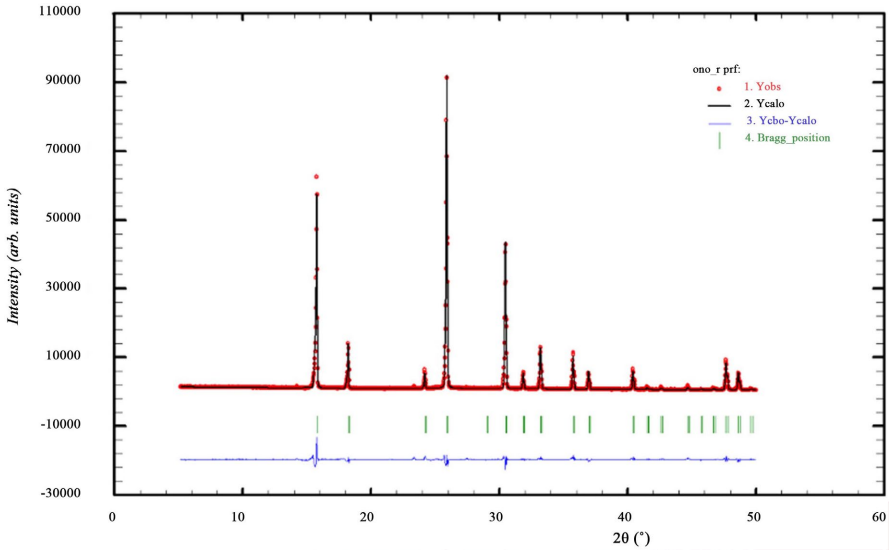

Figure 2. Experimental, calculated XRD pattern and their difference for Rietveld refinement of synthetized zeolite sample.

3.3. Crystallite Size and Lattice Microstrain Estimation

Although 15 reflections were indexed in the XRD pattern, only 12 sufficiently intense reflections were selected for the microstructural analysis. The (620), (541), and (631) reflections were excluded because of their very low intensities, which prevented reliable determination of their FWHM values.

3.3.1. Scherrer and Monschi-Scherrer Methods

The average crystallite size is obtained from the slope of the plot of $\ln\beta$ as a function of $\ln(1/\cos\theta)$. The Scherrer and Monshi-Scherrer methods (Figure 3 and Figure 4) yield crystallite sizes of 56.46-98.84 nm (with an average of 75.47 nm) and 98.71 nm, respectively (Figure 3 and Figure 4).

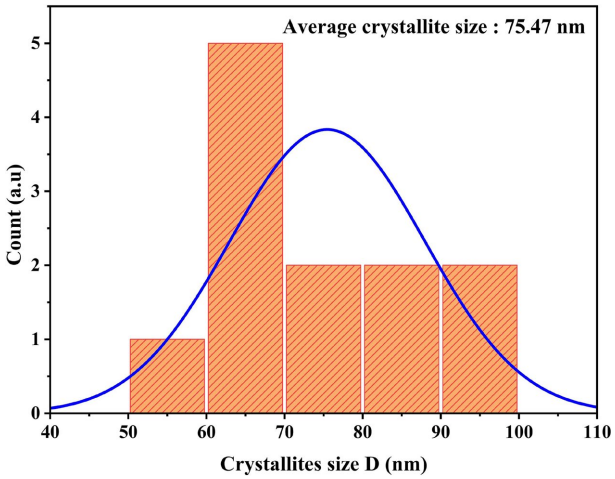

Figure 3. Scherrer method.

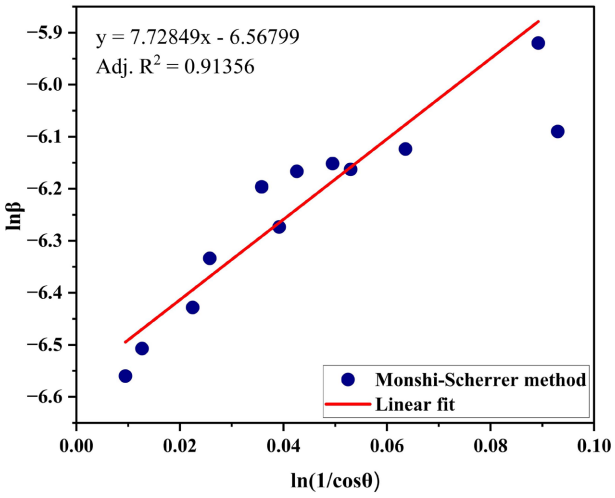

Figure 4. Monshi-Scherrer method.

3.3.2. Williamson-Hall Method

a) Uniform deformation model (UDM)

The linear fit (Figure 5) of $\beta_{hkl}\cdot\cos\theta$ versus $4\sin\theta$ enabled the determina-

tion of the average crystallite size from the intercept ($K\lambda/D$ = 8.74588 × 10^{-4}), while the latiice microstrain was directly obtained from the slope (ε = 9.31 × 10^{-4}). The resulting average crystallite size was found to be 158.54 nm. The positive value of the microstrain indicates that the strain is of a tensile nature [11] [22].

b) Uniform stress deformation model (USDM)

The Young's moduli corresponding to the Miller indices of cubic analcime were calculated using Equation (7) and are reported in **Table 1**. The linear fit of the plot of $\beta_{hkl}\cdot\cos\theta$ versus $4\sin\theta/Y_{hkl}$, shown in **Figure 6**, enabled the average crystallite size to be estimated from the intercept ($K\lambda/D$ = 9.38071 × 10^{-4}). The resulting average crystallite size is approximately 149.46 nm. The slope, corresponding to σ = 0.0698 GPa, was used to determine the lattice microstrain (ε = 9.024 × 10^{-4})

Table 1. Young's moduli corresponding to the Miller indices of cubic analcime.

h	k	l	Y_{hkl} (GPa)
2	1	1	77.369
2	2	0	77.369
3	2	1	77.369
4	0	0	97.182
3	3	2	73.411
4	2	2	77.369
4	3	1	77.369
5	2	1	84.745
4	4	0	77.369
5	3	2	77.369
6	4	0	79.775
6	3	3	77.369

c) Uniform deformation energy density model (UDEDM)

The intercept of the linear fit of the plot of $\beta_{hkl}\cdot\cos\theta$ as a function of $4\sin\theta\cdot\sqrt{\frac{2}{Y_{hkl}}}$ (**Figure 7**), given by $K\cdot\lambda/D$ = 0.0008933, yielded an average crystallite size of approximately 155.21 nm. The slope $\sqrt{u}$ = 0.00575 was used to estimate the anisotropic strain energy density u = 3.306 × 10^{-5} GPa. By rearranging Equation (8), the microstrain value ε was determined to be approximately 9.24 × 10^{-4}, corresponding to a stress of σ = 0.0712 GPa.

3.3.3. Size-Strain Plot Method

The linear fit of the experimental data of the plot of $\left(d_{hkl}^2\cdot\beta_{hkl}\cdot\cos\theta\right)$ versus $\left(d_{hkl}\cdot\beta_{hkl}\cdot\cos\theta\right)^2$, presented in **Figure 8**, enabled the crystallite size and lattice strain to be estimated from the slope ($K\cdot\lambda/D$ = 0.0012) and the intercept ($\varepsilon^2/4$ = 9.80678.10^{-6}), respectively. The calculated crystallite size and lattice strain are 115.54 nm and ε = 6.26 × 10^{-3}, respectively.

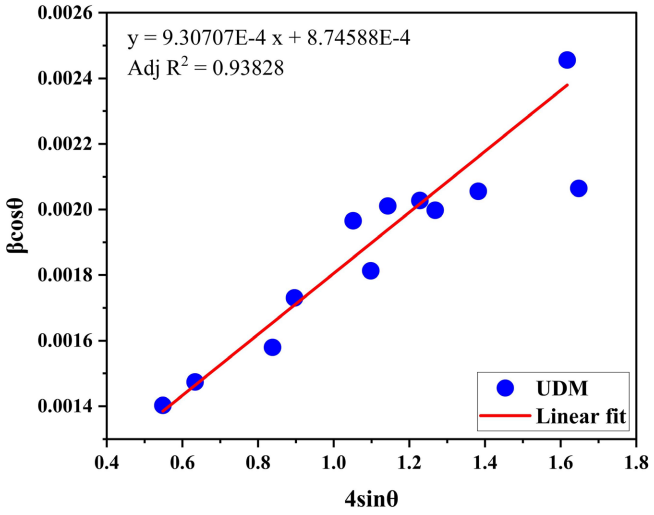

Figure 5. UDM.

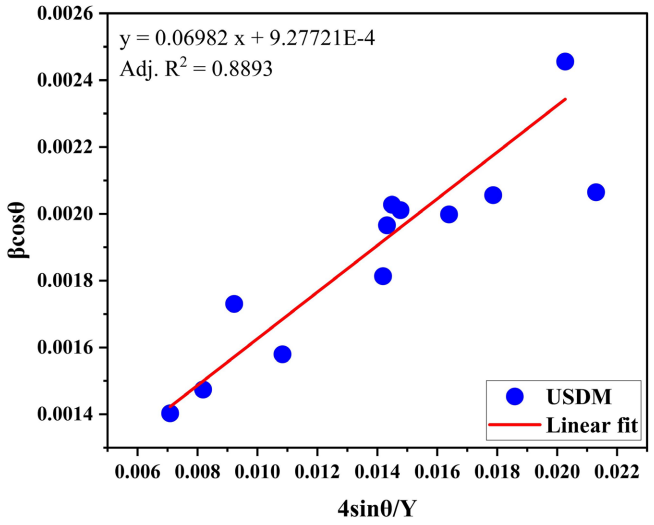

Figure 6. USDM.

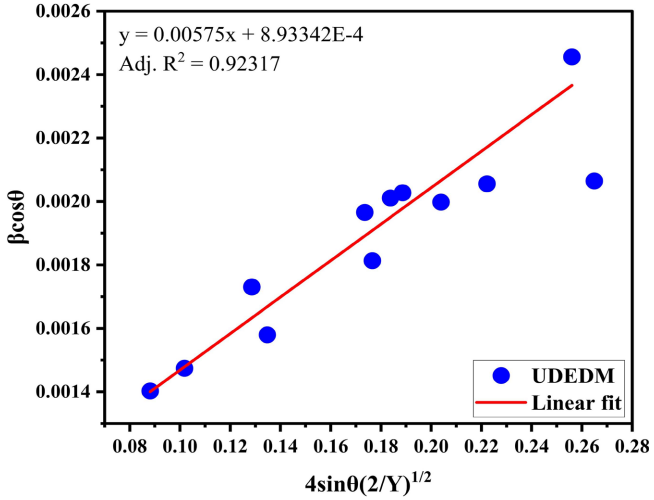

Figure 7. UDEDM.

3.3.4. Halder-Wagner Method

The linear fitting of the plot of $\left(\frac{\beta_{hkl}}{2\tan\theta}\right)^2$ as a function of $\left(\frac{\beta_{hkl}}{4\tan\theta\cdot\sin\theta}\right)$ derived from the experimental data (Figure 9) made it possible to estimate the crystallite size and lattice strain from the slope ($K\lambda/D = 0.0012$) and the intercept ($4\varepsilon^2 = 4.12991 \times 10^{-6}$). The calculated crystallite size and strain are $D = 115.542$ nm and $\varepsilon = 1.02 \times 10^{-3}$, respectively.

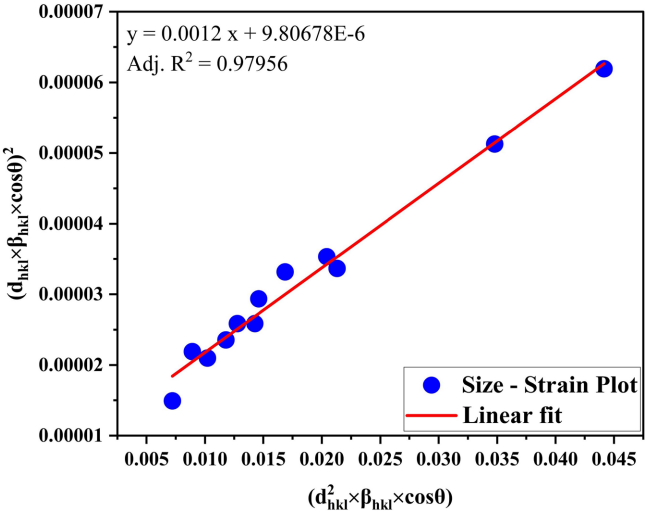

Figure 8. Size-Strain plot.

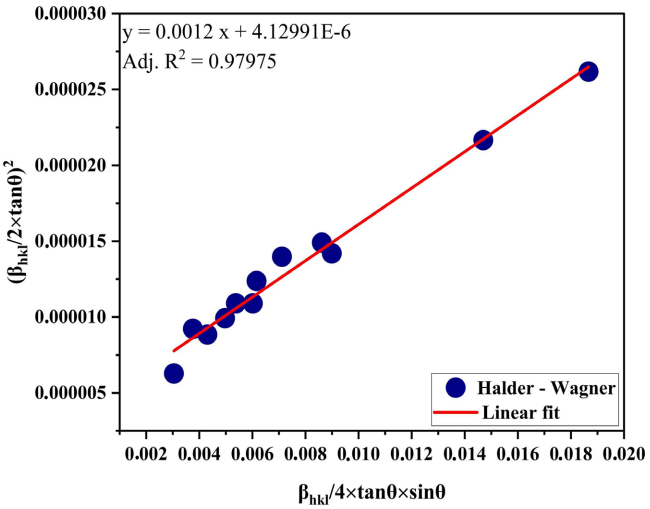

Figure 9. Halder-Wagner.

3.3.5. Modified Warren-Averbach Method

The slope $\lambda/D = 0.0012$ and the intercept ($25\langle\varepsilon^2\rangle = 1.65196\times10^{-4}$), obtained from the linear fit of the plot of $\frac{\beta_{hkl}^2}{\tan\theta}$ versus $\frac{\beta_{hkl}}{\tan\theta\sin\theta}$, as shown in Figure 10, enabled the estimation of crystallite size and lattice strain. The calculated crystallite size and lattice strain are 128.383 nm and 8.13×10^{-4}, respectively.

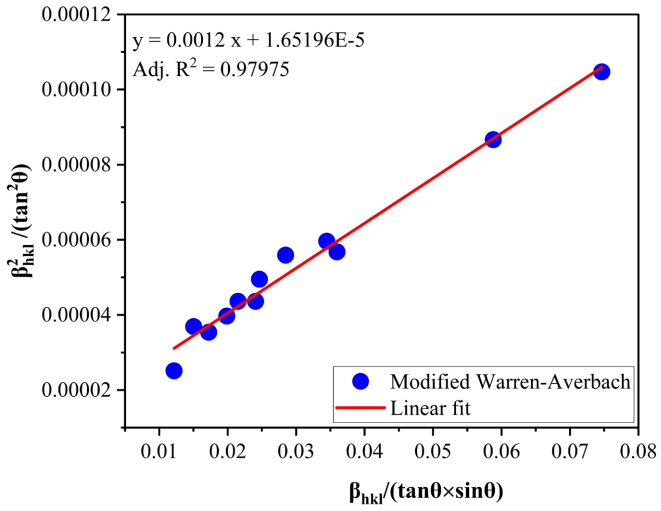

Figure 10. Modified warren-averbach method.

Analysis of the diffraction peak broadening data (**Figure 11**) revealed a pronounced dependence of the crystallite size and lattice microstrain values on the analytical method employed. The estimated crystallite sizes ranged from 75.47 to 158.54 nm, whereas the corresponding microstrain values were on the order of 10^{-4} - 10^{-3}. Similar discrepancies have been widely reported in the literature, demonstrating that these analytical approaches may yield significantly different results for the same material [21] [23] [43]. This variability primarily reflects the distinct theoretical assumptions underlying each method rather than intrinsic differences in the material itself. The Scherrer and Monshi-Scherrer methods produced the smallest crystallite sizes, namely 75.47 and 98.71 nm, respectively, which is consistent with the fact that these approaches neglect the contribution of lattice microstrain [21]. In contrast, the Williamson-Hall models, namely UDM, USDM, UDEDM, yielded the lagest crystallite sizes of 158.54, 149.46, and 155.21 nm, respectively, owing to the explicit separation of size and strain-induced broadening. However, these models rely on assumptions of isotropic deformation (UDM) or simplified elastic approximations (USDM ans UDEDM), with may substantially influence the calculed values. Consequently, these results should be regarded as model-dependent estimates rather than absolute physical quantities. The Size-strain plot and Halder-Wagner methods produced similar crystallite sizes of approximately 115.54 nm, indicating good internal consistency in the treatment of diffraction peak broadening. This agreement suggest that these approches may provide a more realistic estimate of the average coherent domain size [31] [44] in nanocrystalline materials such zeolite. The modified Warren-Averbach method yielded an intermediate crystallite size of 128.38 nm, lying between the estimates obtained using the Scherrer-type and Williamson-Hall approaches. For analcime, these results are consistent with a highly crystalline framework while also indicating the presence of local lattice distortions and point defects [45] [46]. The calculated microstrain values were relatively low, on the order of 10^{-3} -

10^{-4}, and exhibited good consistency in the terms of magnitude. These low indicate the pressence of moderate internal lattice strain while suggesting that the associated structural imperfections remain limited and do not significantly disrupt the long-range crystalline order, in agreement with the overall high crystallinity of the synthesized analcime. Overall, the differences observed among the various analytical methods primarily arise from their underlying modeling assumptions and their intrinsic sensitivity to the respective contributions of crystallite size and lattice strain to diffraction peak broadening. Within this context, the size-strain plot and Halder-Wagner methods appear to provide the most reliable estimates of the average coherent domain size, whereas the Scherrer and Williamson-Hall methods may reasonably be regarded as providing the lower and upper bounds of the crystallite size estimation, respectively. Finally, the crystallite sizes determined in this study should be interpreted as the diffraction coherence domain size, corresponding to the crystal regions that diffract coherently with the synthesized analcime. (**Figure 11**)

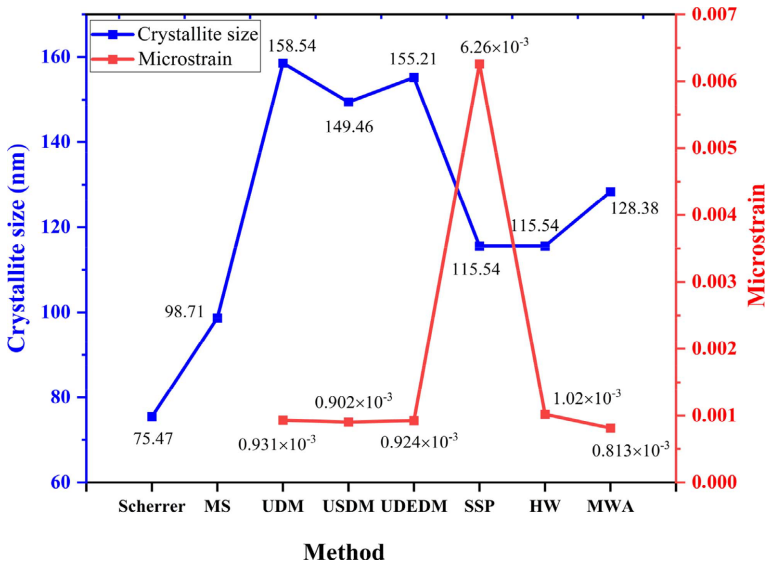

Figure 11. Correlation crystallite size - strain.

3.4. Microscopie Scanning Electron Microscopy Coupled with Energy-Dispersive Spectroscopy

Figure 12 and **Figure 13** present the SEM micrographs and the results of the EDS analysis of the synthesized product. **Figure 12(a)** and **Figure 12(b)** show homogeneous particles with spherical shapes. The observation of **Figure 12(c)** and **Figure 12(d)** shows a trapezohedral or deltoidal icositetrahedral morphology, characteristic of analcime [47]-[49], whose particle size (**Figure 14**) ranges from 6.97 to 14.79 µm, with an average particle size of 11.7 µm (**Figures 12-14**).

3.5. Infrared Spectroscopy

Figure 15 shows the infrared spectrum of the synthesized product, and the observed bands are consistent with those reported in the literature. The band at 619 cm^{-1} is attributed to the T-O-T (T = Si or Al) bending vibration [50] [51]. The

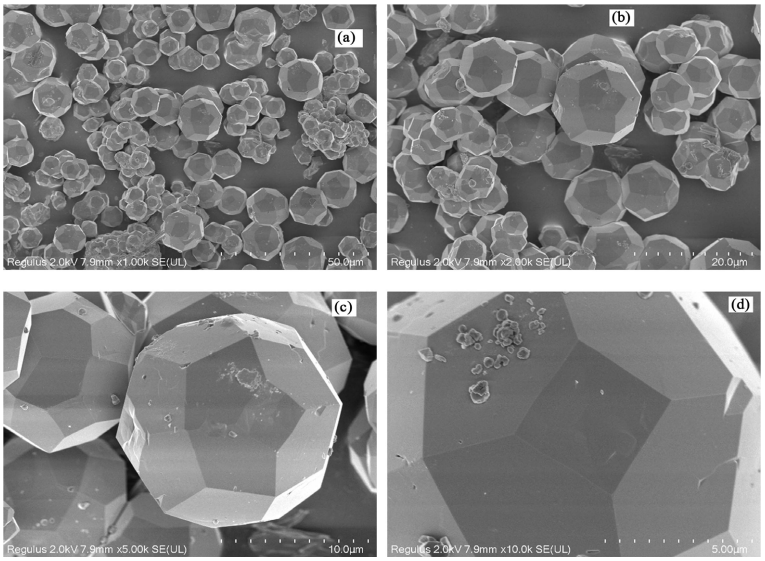

Figure 12. SEM of synthetized Analcime; scale: (a) 50 µm, (b) 20 µm, (c); 10 µm, (d) 5 µm.

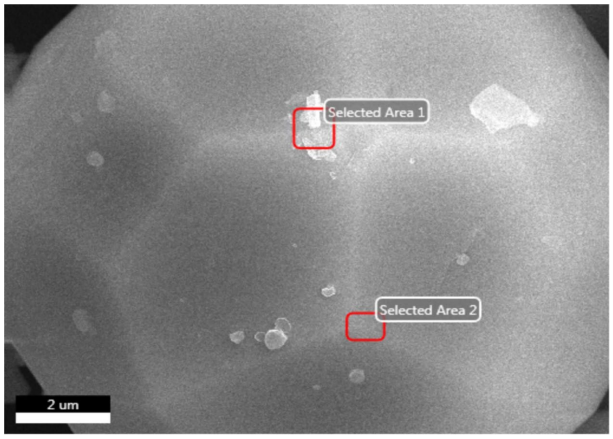

(a)

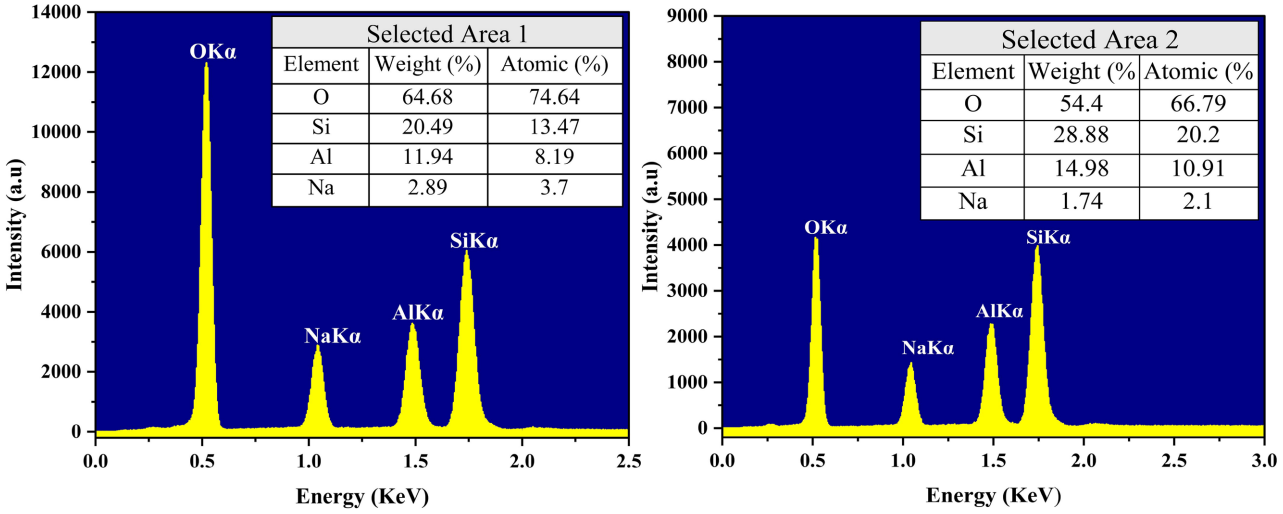

(b) (c)

Figure 13. SEM-EDS of synthetized compound.

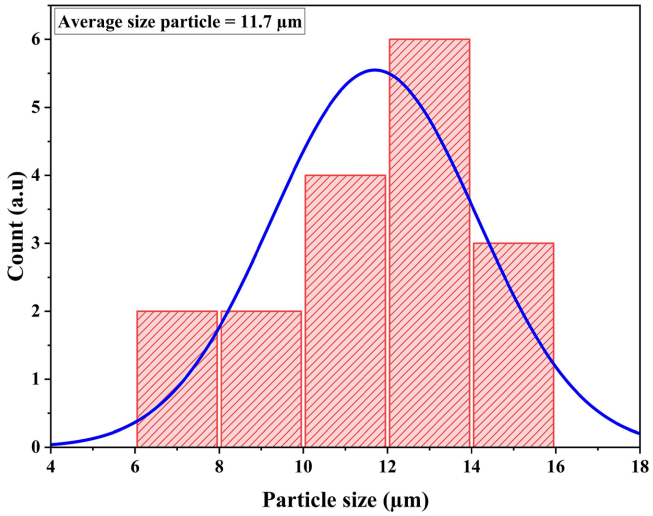

Figure 14. Particle size of the synthesized compound.

band at 730 cm^{-1} corresponds to the external symmetric vibration of T-O-T linkages. The broad band around 965 cm^{-1} is assigned to the asymmetric stretching vibration of T-O bonds [50] [52]. The band at 1633 cm^{-1} is related to the bending vibration of OH groups from water molecules located within the zeolite micropores. In contrast, the absorption band around 3599 cm^{-1} is associated with the O-H stretching vibration of silanol groups and adsorbed water molecules [50] [52] [53].

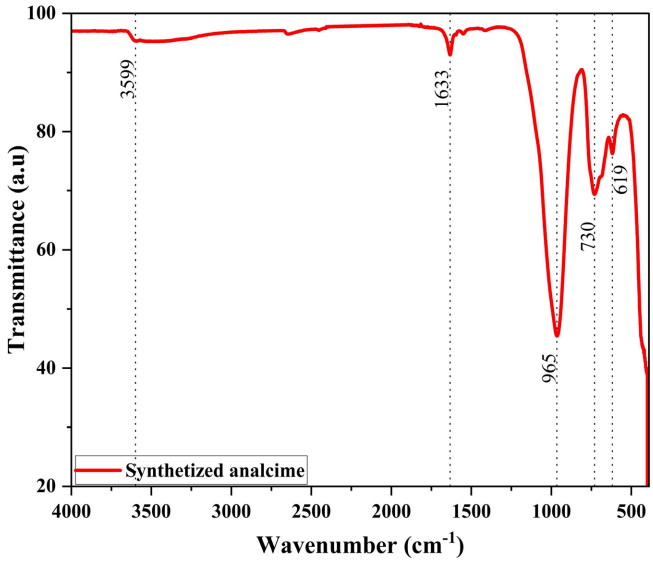

Figure 15. Infrared spectrum of the synthesized compound.

3.6. X-Ray Fluorescence

Figure 16 presents the chemical composition of the synthesized product. The data indicate that the material is predominantly an aluminosilicate, with a high silicon content or silica (Si: 61.9% or SiO_2: 58.9%). The proportions of aluminum or alu-

mina (Al: 22.2% or Al_2O_3: 24.2%) and sodium or sodium oxide (15.3% or Na_2O: 16.7%) are also significant. The Si/Al ratio of 2.8 suggests the formation of an analcime-type zeolite [54].

4. Conclusion

In this study, a zeolitic powder was synthesized via a hydrothermal route at 105˚C. The obtained powder was characterized using X-ray diffraction (XRD), scanning electron microscopy coupled with energy-dispersive spectroscopy (SEM-EDS), infrared spectroscopy (IR), and X-ray fluorescence (XRF). The XRD analysis revealed that the synthesized compound crystallizes in a cubic system with the space group Ia-3d. SEM-EDS, FTIR, and XRF analyses confirmed the formation

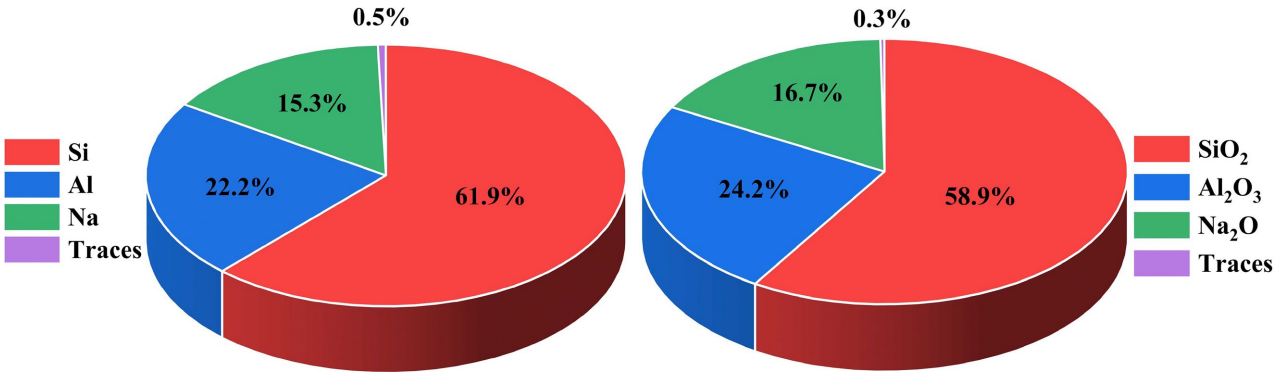

(a) elemental composition (b) oxide composition

Figure 16. Chemical composition of the compound synthesized.

of analcime. The Scherrer and Monshi-Scherrer methods yielded crystallite sizes ranging from 75.47 nm to 98.71 nm. The Williamson-Hall method, using the uniform deformation model (UDM), uniform stress deformation model (USDM), and uniform deformation energy density model (UDEDM), provided crystallite sizes of 158.54 nm, 149.46 nm, and 155.21 nm, respectively, along with corresponding microstrains of 0.931×10^{-3}, 0.902×10^{-3}, and 0.924×10^{-3}. Furthermore, the Halder-Wagner, size-strain plot, and modified Warren-Averbach methods yielded crystallite sizes of 115.54 nm, 115.54 nm, and 128.38 nm, respectively, with associated microstrains of 1.02×10^{-3}, 6.26×10^{-3}, and 8.13×10^{-4}. Overall, this study demonstrates that both crystallite size and microstrain are strongly dependent on the analytical method used.

Author Contributions

Ferland Ngoro-elenga: conceptualisation, data curation, methodology, writing-original draft and writing-reviews and editing; Merveilla Bounzi: methodology; Fernand Atipo Itoua Ngopoh and Eric Ziki: writing-review and editing; Hilaire Elenga, Timothée Nsongo: validation, supervision. All authors have read and approved the final version of the manuscript.

Data Availability Statement

All data generated or analyzed during this study are included in the published article.

Acknowledgements

The authors express their gratitude to the Director General of the Geological and Mining Research Center (CRGM) of the Republic of the Congo for technical and administrative support.

Conflicts of Interest

The authors declare that they have no conflict of interest.

References

[1] Pérez-Botella, E., Valencia, S. and Rey, F. (2022) Zeolites in Adsorption Processes: State of the Art and Future Prospects. *Chemical Reviews*, **122**, 17647-17695. https://doi.org/10.1021/acs.chemrev.2c00140

[2] Novembre, D. and Gimeno, D. (2021) Synthesis and Characterization of Analcime (ANA) Zeolite Using a Kaolinitic Rock. *Scientific Reports*, **11**, Article No. 13373. https://doi.org/10.1038/s41598-021-92862-0

[3] Li, A., Li, P., Yue, X., Huang, Z., Zhang, J., Tan, W., *et al.* (2025) Analcime Zeolite Synthesis from the Bottom Ash of Co-Incinerated Industrial Hazardous and Medical Waste for Tetracycline Removal from Wastewater. *RSC Advances*, **15**, 27076-27083. https://doi.org/10.1039/d5ra01328c

[4] Bortolini, H.R., Lima, D.S. and Perez-Lopez, O.W. (2020) Hydrothermal Synthesis of Analcime without Template. *Journal of Crystal Growth*, **532**, Article ID: 125424. https://doi.org/10.1016/j.jcrysgro.2019.125424

[5] Bai, R., Song, Y., Lätsch, L., Zou, Y., Feng, Z., Copéret, C., *et al.* (2022) Switching between Classical/Nonclassical Crystallization Pathways of TS-1 Zeolite: Implication on Titanium Distribution and Catalysis. *Chemical Science*, **13**, 10868-10877. https://doi.org/10.1039/d2sc02679a

[6] Zi, W., Hu, Z., Jiang, X., Zhang, J., Guo, C., Qu, K., *et al.* (2023) Morphology Regulation of Zeolite MWW via Classical/Nonclassical Crystallization Pathways. *Molecules*, **29**, Article No. 170. https://doi.org/10.3390/molecules29010170

[7] Yu, J., Du, K., Pan, D., Li, H., Ding, L., Chen, W., *et al.* (2025) Distinguishing and Unraveling Classical and Non-Classical Pathways in MFI Zeolite Crystallization: Insights into Their Contributions and Impact on the Final Product. *Inorganic Chemistry Frontiers*, **12**, 4048-4058. https://doi.org/10.1039/d5qi00224a

[8] Chu-Jon, C., Martinez, E., Bertolazzo, A.A., Koneru, A., Sankaranarayanan, S.K.R.S., Rimer, J.D., *et al.* (2025) From Nonclassical to Classical: Crystallization Seeds Reshape Nucleation Mechanisms. *Journal of the American Chemical Society*, **147**, 20456-20465. https://doi.org/10.1021/jacs.5c02580

[9] Hameed, A.M., Alharbi, A., Abdelrahman, E.A., Mabrouk, E.M., Hegazey, R.M., Algethami, F.K., *et al.* (2020) Facile Hydrothermal Fabrication of Analcime and Zeolite X for Efficient Removal of Cd(II) Ions from Aqueous Media and Polluted Water. *Journal of Inorganic and Organometallic Polymers and Materials*, **30**, 4117-4128. https://doi.org/10.1007/s10904-020-01565-y

[10] Kawsar, M., Hossain, M.S., Bahadur, N.M. and Ahmed, S. (2024) Synthesis of Nano-Crystallite Hydroxyapatites in Different Media and a Comparative Study for Estimation of Crystallite Size Using Scherrer Method, Halder-Wagner Method Size-Strain Plot, and Williamson-Hall Model. *Heliyon*, **10**, e25347. https://doi.org/10.1016/j.heliyon.2024.e25347

[11] Rabiei, M., Palevicius, A., Monshi, A., Nasiri, S., Vilkauskas, A. and Janusas, G. (2020) Comparing Methods for Calculating Nano Crystal Size of Natural Hydroxyapatite Using X-Ray Diffraction. *Nanomaterials*, **10**, Article No. 1627. https://doi.org/10.3390/nano10091627

[12] Disha, S.A., Sahadat Hossain, M., Habib, M.L. and Ahmed, S. (2024) Calculation of Crystallite Sizes of Pure and Metals Doped Hydroxyapatite Engaging Scherrer Method, Halder-Wagner Method, Williamson-Hall Model, and Size-Strain Plot. *Results in Materials*, **21**, Article ID: 100496. https://doi.org/10.1016/j.rinma.2023.100496

[13] Desai, K.R., Alone, S.T., Wadgane, S.R., Shirsath, S.E., Batoo, K.M., Imran, A., *et al.* (2021) X-Ray Diffraction Based Williamson-Hall Analysis and Rietveld Refinement for Strain Mechanism in Mg-Mn Co-Substituted $CdFe_2O_4$ Nanoparticles. *Physica B: Condensed Matter*, **614**, Article ID: 413054. https://doi.org/10.1016/j.physb.2021.413054

[14] Nath, D., Singh, F. and Das, R. (2020) X-Ray Diffraction Analysis by Williamson-Hall, Halder-Wagner and Size-Strain Plot Methods of CdSe Nanoparticles—A Comparative Study. *Materials Chemistry and Physics*, **239**, Article ID: 122021. https://doi.org/10.1016/j.matchemphys.2019.122021

[15] Prabhu, Y.T., Rao, K.V., Kumar, V.S.S. and Kumari, B.S. (2014) X-Ray Analysis by Williamson-Hall and Size-Strain Plot Methods of ZnO Nanoparticles with Fuel Variation. *World Journal of Nano Science and Engineering*, **4**, 21-28. https://doi.org/10.4236/wjnse.2014.41004

[16] Madisetti, D., Sudmanns, M., Stiles, C.D. and El-Awady, J.A. (2025) Computational Investigation into XRD Peak Broadening Effects with Discrete Dislocation Dynamics in Additively Manufactured 316L Stainless Steel. *Journal of the Mechanics and Physics of Solids*, **196**, Article ID: 105970. https://doi.org/10.1016/j.jmps.2024.105970

[17] Ivanov, I.V., Emurlaev, K.I., Kuper, K.E., Akkuzin, S.A. and Bataev, I.A. (2022) Deconvolution-Based Peak Profile Analysis Methods for Characterization of CoCrFeMnNi High-Entropy Alloy. *Heliyon*, **8**, e10541. https://doi.org/10.1016/j.heliyon.2022.e10541

[18] Muiruri, A., Maringa, M. and du Preez, W. (2020) Evaluation of Dislocation Densities in Various Microstructures of Additively Manufactured Ti_6Al_4V (Eli) by the Method of X-Ray Diffraction. *Materials*, **13**, Article No. 5355. https://doi.org/10.3390/ma13235355

[19] Almirón, J., Churata, R., Vargas, M., Roudet, F., Valverde-Ponce, K., Gordillo-Andia, C., *et al.* (2025) Hydrothermal Synthesis of Zeolites from Volcanic Ash from Ubinas and Its Application in Catalytic Pyrolysis of Plastic Waste. *Processes*, **13**, Article No. 3376. https://doi.org/10.3390/pr13113376

[20] Hassanzadeh-Tabrizi, S.A. (2023) Precise Calculation of Crystallite Size of Nanomaterials: A Review. *Journal of Alloys and Compounds*, **968**, Article ID: 171914. https://doi.org/10.1016/j.jallcom.2023.171914

[21] Jannat, M.R., Biswas, B., Rahman, M.L., Ahmed, M.F., Hossain, M.J., Khanam, J., *et al.* (2025) Validity of Crystallite Size Determination Methods Based on XRD Peak Broadening in Pure and Metal-Doped Nickel Ferrites. *Results in Materials*, **28**, Article

ID: 100762. https://doi.org/10.1016/j.rinma.2025.100762

[22] Manh, D.H., Ngoc Nha, T.T., Hong Phong, L.T., Nam, P.H., Thanh, T.D. and Phong, P.T. (2023) Determination of the Crystalline Size of Hexagonal $La_{1-x}Sr_xMnO_3$ (x = 0.3) Nanoparticles from X-Ray Diffraction—A Comparative Study. *RSC Advances*, **13**, 25007-25017. https://doi.org/10.1039/d3ra04018f

[23] Ateia, E.E., Reda, M., El-Dek, S.I. and Arman, M.M. (2024) A Comparative Approach for Estimating Microstructural Characteristics of $BaTi_{1-x}Zr_xO_3$ ($0.0 \leq X \leq 0.3$) Nanoparticles via X-Ray Diffraction Patterns. *Journal of Sol-Gel Science and Technology*, **110**, 887-899. https://doi.org/10.1007/s10971-024-06389-7

[24] Bindu, P. and Thomas, S. (2014) Estimation of Lattice Strain in ZnO Nanoparticles: X-Ray Peak Profile Analysis. *Journal of Theoretical and Applied Physics*, **8**, 123-134. https://doi.org/10.1007/s40094-014-0141-9

[25] Sanchez-Valle, C., Sinogeikin, S.V., Lethbridge, Z.A.D., Walton, R.I., Smith, C.W., Evans, K.E., *et al.* (2005) Brillouin Scattering Study on the Single-Crystal Elastic Properties of Natrolite and Analcime Zeolites. *Journal of Applied Physics*, **98**, Article ID: 053508. https://doi.org/10.1063/1.2014932

[26] Lethbridge, Z.A.D., Walton, R.I., Bosak, A. and Krisch, M. (2009) Single-Crystal Elastic Constants of the Zeolite Analcime Measured by Inelastic X-Ray Scattering. *Chemical Physics Letters*, **471**, 286-289. https://doi.org/10.1016/j.cplett.2009.02.060

[27] Mote, V.D., Purushotham, Y. and Dole, B. (2012) Williamson-Hall Analysis in Estimation of Lattice Strain in Nanometer-Sized ZnO Particles. *Journal of Theoretical and Applied Physics*, **6**, 1-8. https://doi.org/10.1186/2251-7235-6-6

[28] Alam, S., Bashar, M.S., Bhuiyan, M.M.R., Kabir, M.A., Neher, B. and Ahmed, F. (2026) Comprehensive Study on the Impact of A-Site Cation Engineering on Crystallite Growth, Strain, and Defect Dynamics in Lead Bromide Perovskite Nanostructures and Thin Films. *Results in Materials*, **30**, Article ID: 100938. https://doi.org/10.1016/j.rinma.2026.100938

[29] Halder, N.C. and Wagner, C.N.J. (1966) Separation of Particle Size and Lattice Strain in Integral Breadth Measurements. *Acta Crystallographica*, **20**, 312-313. https://doi.org/10.1107/s0365110x66000628

[30] Balzar, D. and Ledbetter, H. (1993) Voigt-Function Modeling in Fourier Analysis of Size- and Strain-Broadened X-Ray Diffraction Peaks. *Journal of Applied Crystallography*, **26**, 97-103. https://doi.org/10.1107/s0021889892008987

[31] Madansure, Y.S., Gurav, S.K., Balsure, S.D., Gaikwad, P.K., Imran, A., El-Toni, A.M., *et al.* (2026) X-Ray Diffraction Analysis by Williamson-Hall, Strain-Size, Halder-Wagner, and Nelson-Riley Methods, and Its Co-Relationship with Elastic and Magnetic Properties of Ce^{3+} Substituted Fe-Rich Cobalt Ferrite. *Journal of Materials Science: Materials in Electronics*, **37**, Article No. 706. https://doi.org/10.1007/s10854-026-17126-x

[32] Morán, M., Álvarez, M.V., Vizcaíno, P., Brown, D.W. and Santisteban, J. (2022) Dislocation Density Evolution in Cold-Rolled Zr-2.5%Nb Pressure Tubes under Thermal Treatments by High Energy XRD and Neutron TOF Diffraction Peak Profile Analysis. *Journal of Alloys and Compounds*, **929**, Article ID: 167196. https://doi.org/10.1016/j.jallcom.2022.167196

[33] Cho, C., Son, K. and Cho, H. (2023) Experimental Analysis of Deformation Texture Evolutions in Pure Cu, Cu-37Zn, Al-6Mg, and -8Mg Alloys at Cold-Rolling Processes. *Journal of Alloys and Compounds*, **934**, Article ID: 167879. https://doi.org/10.1016/j.jallcom.2022.167879

[34] Cho, C.-H., Lee, J.-W., Son, K.-T. and Hyum, S.-K. (2021) Strain Rate Effects on Microstructure and Texture Evolution in Cold-Sheared Al-6Mg Alloys during Low-Temperature Annealing. *Journal of Alloys and Compounds*, **889**, Article ID: 161630. https://doi.org/10.1016/j.jallcom.2021.161630

[35] Youssef, K.M., Scattergood, R.O., Murty, K.L. and Koch, C.C. (2006) Nanocrystalline Al-Mg Alloy with Ultrahigh Strength and Good Ductility. *Scripta Materialia*, **54**, 251-256. https://doi.org/10.1016/j.scriptamat.2005.09.028

[36] El-Makaty, F.M., Andre Mkhoyan, K. and Youssef, K.M. (2021) The Effects of Structural Integrity of Graphene on the Thermoelectric Properties of the N-Type Bismuth-Telluride Alloy. *Journal of Alloys and Compounds*, **876**, Article ID: 160198. https://doi.org/10.1016/j.jallcom.2021.160198

[37] Abdelrahman, E.A., Alqahtani, Z., Abou-Krisha, M.M., Saad, F.A. and Shah, R.K. (2025) Facile Synthesis and Characterization of Novel Analcime/Sodium Magnesium Aluminum Silicon Silicate Nanocomposite for Efficient Removal of Methylene Blue Dye from Aqueous Media. *Molecules*, **30**, Article No. 1488. https://doi.org/10.3390/molecules30071488

[38] Jiménez, A., Misol, A., Morato, Á., Rives, V., Vicente, M.A. and Gil, A. (2021) Synthesis of Pollucite and Analcime Zeolites by Recovering Aluminum from a Saline Slag. *Journal of Cleaner Production*, **297**, Article ID: 126667. https://doi.org/10.1016/j.jclepro.2021.126667

[39] Saville, A.I., Creuziger, A., Mitchell, E.B., Vogel, S.C., Benzing, J.T., Klemm-Toole, J., *et al.* (2021) MAUD Rietveld Refinement Software for Neutron Diffraction Texture Studies of Single- and Dual-Phase Materials. *Integrating Materials and Manufacturing Innovation*, **10**, 461-487. https://doi.org/10.1007/s40192-021-00224-5

[40] Singh, V., Batra, S. and Bhushan Sharma, I. (2020) Rietveld Analysis for Crystal Structure Determination of Polycrystalline Materials. *Materials Today*: *Proceedings*, **29**, 832-835. https://doi.org/10.1016/j.matpr.2020.04.867

[41] Runčevski, T. and Brown, C.M. (2021) The Rietveld Refinement Method: Half of a Century Anniversary. *Crystal Growth & Design*, **21**, 4821-4822. https://doi.org/10.1021/acs.cgd.1c00854

[42] Gregorkiewitz, M. and Boschetti, A. (2024) Lattice Symmetry Relaxation as a Cause for Anisotropic Line Broadening and Peak Shift in Powder Diffraction. *Acta Crystallographica Section A Foundations and Advances*, **80**, 439-445. https://doi.org/10.1107/s2053273324008799

[43] Khorsand Zak, A. and Hashim, A.M. (2026) Advanced XRD Peak Broadening Analysis of Gallium-Doped ZnO Nanoparticles for Crystallite Size Evaluation. *Scientific Reports*, **16**, Article No. 1717. https://doi.org/10.1038/s41598-025-31317-2

[44] Basak, M., Rahman, M.L., Ahmed, M.F., Biswas, B. and Sharmin, N. (2022) The Use of X-Ray Diffraction Peak Profile Analysis to Determine the Structural Parameters of Cobalt Ferrite Nanoparticles Using Debye-Scherrer, Williamson-Hall, Halder-Wagner and Size-Strain Plot: Different Precipitating Agent Approach. *Journal of Alloys and Compounds*, **895**, Article ID: 162694. https://doi.org/10.1016/j.jallcom.2021.162694

[45] Mallette, A.J., Shilpa, K. and Rimer, J.D. (2024) The Current Understanding of Mechanistic Pathways in Zeolite Crystallization. *Chemical Reviews*, **124**, 3416-3493. https://doi.org/10.1021/acs.chemrev.3c00801

[46] Asgar Pour, Z., Alassmy, Y.A. and Sebakhy, K.O. (2023) A Survey on Zeolite Synthesis and the Crystallization Process: Mechanism of Nucleation and Growth Steps. *Crystals*, **13**, Article No. 959. https://doi.org/10.3390/cryst13060959

[47] Larpkasemsuk, A., Chuayjuljit, S., Kornpanom, W. and Kashima, D.P. (2013) Hydrothermal Synthesis of Analcime from Local Pottery Stone. *Advanced Materials Research*, **664**, 801-805. https://doi.org/10.4028/www.scientific.net/amr.664.801

[48] Mameli, P., Fiore, A.M., Fiore, S. and Huertas, F.J. (2025) Mechanism of Hydrothermal Zeolite Crystallization from Kaolin in Concentrated NaOH Solutions (1-5 M): Formation of NaP1, NaP2, Analcime, Sodalite and Cancrinite. *Crystals*, **15**, Article No. 980. https://doi.org/10.3390/cryst15110980

[49] Sun, L., Xu, X., Sun, D., Chu, S., Chen, J., Shi, W., *et al.* (2022) Synthesis of Large Single Crystals of Analcime in a Template-Free System. *CrystEngComm*, **24**, 4013-4020. https://doi.org/10.1039/d2ce00338d

[50] de Magalhães, L.F., da Silva, G.R., Henriques, A.B., de Freitas, V.A.A. and Peres, A.E.C. (2024) Synthesis of Analcime Zeolite from Glass Powder Waste and Aluminium Anodizing Waste. *Silicon*, **16**, 4173-4185. https://doi.org/10.1007/s12633-024-02992-z

[51] Abdelrahman, E.A., Alharbi, A., Subaihi, A., Hameed, A.M., Almutairi, M.A., Algethami, F.K., *et al.* (2020) Facile Fabrication of Novel Analcime/Sodium Aluminum Silicate Hydrate and Zeolite Y/Faujasite Mesoporous Nanocomposites for Efficient Removal of Cu(II) and Pb(II) Ions from Aqueous Media. *Journal of Materials Research and Technology*, **9**, 7900-7914. https://doi.org/10.1016/j.jmrt.2020.05.052

[52] Iqbal, A., Sattar, H., Haider, R. and Munir, S. (2019) Synthesis and Characterization of Pure Phase Zeolite 4A from Coal Fly Ash. *Journal of Cleaner Production*, **219**, 258-267. https://doi.org/10.1016/j.jclepro.2019.02.066

[53] Byrappa, K. and Suresh Kumar, B.V. (2007) Characterization of Zeolites by Infrared Spectroscopy. *Asian Journal of Chemistry*, **19**, 4933-4935.

[54] Vereshchagina, T.A., Kutikhina, E.A., Solovyov, L.A., Vereshchagin, S.N., Mazurova, E.V., Chernykh, Y.Y., *et al.* (2018) Synthesis and Structure of Analcime and Analcime-Zirconia Composite Derived from Coal Fly Ash Cenospheres. *Microporous and Mesoporous Materials*, **258**, 228-235. https://doi.org/10.1016/j.micromeso.2017.09.011